ADVANCED ENERGY MATERIALS
www.advenergymat.de

Template-Assisted Growth of $Cs_xFA_{1-x}PbI_3$ with Pulsed Laser Deposition for Single Junction Perovskite Solar Cells

*Suzana Kralj, Kerem Artuk, Alexander Wieczorek, Nikolai Orlov, Zeinab Eftekhari, Rebecca Saive, Erik Garnett, Sebastian Siol, Christian M. Wolff, and Monica Morales-Masis**

Cesium-formamidinium lead iodide ($Cs_xFA_{1-x}PbI_3$) perovskites are a promising methylammonium-free alternative for efficient single-junction solar cells. However, they have not been fully explored by vapor-phase deposition techniques. Herein, a template-assisted approach is demonstrated for the growth of $Cs_xFA_{1-x}PbI_3$ perovskite films using pulsed laser deposition (PLD) from a single-source target of mixed precursors. Implementing a lead iodide (PbI_2) + $Cs_xFA_{1-x}PbI_3$ tailored template, phase-pure $Cs_xFA_{1-x}PbI_3$ films with uniform coverage on both planar and textured substrates are achieved. Compositional analysis via X-ray fluorescence confirms near-stoichiometric transfer of the inorganic cations (Cs/Pb), with identical $Cs_{0.2}FA_{0.8}PbI_3$ composition and a bandgap of 1.58 eV achieved in templated and non-templated films. However, the presence of the template proves essential for attaining phase-pure films in the photoactive cubic (α-) phase. Proof-of-concept solar cells fabricated with templated-PLD α-$Cs_xFA_{1-x}PbI_3$ achieve an efficiency exceeding 12.9% on 0.1 cm^2 area devices without the employment of passivation approaches. Additionally, increasing deposition rates does not alter the phase, morphology, or optoelectronic properties of the templated films on textured substrates, indicating the robustness of this methodology. The compositional control of PLD for Cs-FA-based perovskites is showcased, and template-assisted growth is demonstrated as a reliable pathway to high-quality reproducible perovskite films.

1. Introduction

Since their introduction, metal halide perovskites (MHPs) garnered significant interest of the scientific community for solar cell applications, with the initial focus on methylammonium lead iodide ($MAPbI_3$).[1] However, $MAPbI_3$'s susceptibility to moisture and thermal degradation spurred the exploration of alternative compositions with improved stability. Among these, formamidinium lead iodide ($FAPbI_3$) emerged as a promising candidate due to its increased thermal stability characteristics and an optimal bandgap of 1.48 eV, which is near to the theoretical maximum power conversion efficiency for a single-junction device.[2–6] One of the material's drawbacks, are the observed structural instability and polymorphism, where solid-solid phase transitions near room temperature cause shifting the preferred photoactive cubic (α-) phases to photoinactive (δ-) phases.[7] To further enhance phase stability and bandgap tuning, researchers have alloyed formamidinium (FA)-based compounds with the smaller cesium (Cs^+) cation, resulting in mixed cation Cs-FA compounds.[7–10] These cesium-formamidinium-based absorbers ($Cs_xFA_{1-x}PbI_3$) exhibit shifted bandgap values, falling between the 1.48 eV of $FAPbI_3$ and 1.77 eV of cesium lead iodide ($CsPbI_3$l), depending on the cesium content (x).[3] Furthermore, they show a great potential for efficient and stable single-junction

S. Kralj, Z. Eftekhari, R. Saive, M. Morales-Masis
MESA+ Institute for Nanotechnology
University of Twente
Enschede 7500 AE, The Netherlands
E-mail: m.moralesmasis@utwente.nl

K. Artuk, C. M. Wolff
École Polytechnique Fédérale de Lausanne (EPFL)
Institute of Electrical and Microengineering (IEM)
Photovoltaics and Thin-Film Electronics Laboratory (PV-Lab)
Neuchâtel 2000, Switzerland

A. Wieczorek, S. Siol
Laboratory for Surface Science and Coating Technologies
Empa—Swiss Federal Laboratories for Materials Science and Technology
Duebendorf 8600, Switzerland

N. Orlov, E. Garnett
Center for Nanophotonics
AMOLF
Science Park 104, Amsterdam 1098 XG, The Netherlands

E. Garnett
Van der Waals-Zeeman Institute
University of Amsterdam
Science Park 904, Amsterdam 1098 XH, The Netherlands

The ORCID identification number(s) for the author(s) of this article can be found under https://doi.org/10.1002/aenm.202406033

DOI: 10.1002/aenm.202406033

perovskite solar cells. Devices based on solution-processed $Cs_xFA_{1-x}PbI_3$ have recently achieved over 26% efficiency on a laboratory scale, approaching the current record efficiency for single junction devices.[11,12] Vapor-phase deposition methods for MHP films are also interesting as solvent-free approaches. Yet, the stoichiometric control of complex compositions such as deposited $Cs_xFA_{1-x}PbI_3$ presents challenges for vapor-phase growth.[13,14]

Vapor-phase deposition methods allow for conformal coverage, avoid the use of toxic solvents and several vapor deposition methods have the potential for scalability.[14] The state-of-the-art vapor-phase deposited $Cs_xFA_{1-x}PbI_3$ are summarized in Table S1 (Supporting Information). Most commonly, these processes employ multi-source deposition methods, which include either the simultaneous deposition of multiple individual precursors (co-evaporation),[15–19] or are based on the sequential deposition approach where first inorganic layer is deposited followed by the organic salt deposition.[18,20–22] An alternative process includes a single-source evaporation of MHPs. This has been reported for $Cs_xFA_{1-x}PbI_3$ powders synthesized by solution process and subsequently evaporated via thermal evaporation on flash source evaporation.[23,24] Single-source deposition methods have been highlighted as an approach to simplify the deposition process.[14]

Achieving precise control over Cs and FA stoichiometry, while stabilizing the photoactive cubic (α-) phase, remains a significant challenge in optimizing $Cs_xFA_{1-x}PbI_3$ absorbers.[19,25,26] Solution processing methods have addressed these issues by controlling crystallization dynamics, using additives in the precursor solution, and employing passivation techniques, enabling improvements in composition uniformity and stability.[10,11,27] To suppress the δ-phase formation, a common approach both in solution and vapor deposition is to incorporate excess of formamidinium iodide (FAI) in the source.[4,15,19,28–30] However, using a large excess of organics has been shown to negatively impact device performance.[19,31] Vapor phase deposition methods introduce an additional complexity due to the significant influence of substrate surface properties on composition and bulk film characteristics.[29,31–33] For instance, *Olthof and Meerholz* demonstrated that, during vacuum deposition, the substrate can significantly impact film formation, even initiating interfacial chemical reactions that delay perovskite growth.[32] *Roß et al.* showed the dependence of the substrate temperature and hole-transport layer on the morphology, composition, and performance of absorber layers and devices. Later, Abzieher et al. extended the research on a variety of commonly used hole-selective layers and reported that substrate characteristics influence not only the morphology but also the integration of organohalides into the perovskite framework. This effect, in turn, alters the crystallographic orientation, morphological properties, and composition, potentially leading to deviations from stoichiometry. They further correlated these changes with the polarity of the substrate surface.[33] Even substrates of the same type can exhibit significant variability in film properties due to surface interactions, as demonstrated in recent studies on a phosphonic acid carbazole-based self-assembled monolayer (PACz SAM) transport layers and co-evaporated perovskite interactions.[19,25,26] Feeney et al. noted that SAMs can affect FA content within the film due to exposed phosphonic acids (PA), which form hydrogen bonds and introduce an energy barrier, inhibiting the conversion from α- to δ-phase.[19] Similarly, Castro-Mendez et al. observed PA diffusion during growth, attributing it to a mechanism that stabilizes the α-phase.[25]

The impact of substrate interactions on perovskite film properties in vapor-phase deposition methods has led to the development of alternative growth strategies. To address compositional imbalances, and phase stability, strategies such as using excess organohalide precursors,[28] or adjusting precursors evaporation rates,[19] have shown promise. However, to effectively decouple nucleation and growth from substrate-dependent variability, more robust approaches are needed. These include introducing inorganic seeding layers,[18,34] or the use of templating approach to direct the growth.[16,35] Latter strategies typically start with the deposition of a thin inorganic precursor layer, followed by a thin organic precursor layer, often coupled with an annealing step prior to completing the full perovskite absorber layer. This sequential method, pioneered by S. Yan et al.,[16] has proven as an effective strategy in obtaining identical optoelectronic properties, morphology, and structure of co-evaporated perovskite regardless of the substrate choice.[35]

Motivated by the recent developments in the field of Cs-FA-based perovskites, in this work, we evaluate the potential of pulsed laser deposition (PLD) as a dry, single-source method for the growth of $Cs_xFA_{1-x}PbI_3$ perovskites. This fully solvent-free approach is achievable when combined with synthesis methods like mechanochemical preparation of the starting material.[36–38] The main benefit is that PLD allows the transfer of multi-elemental materials in a near-stoichiometric and controlled manner.[39] This is achieved through the unique thermal and non-equilibrium processes that occur during the laser ablation of the target.[39,40] Those processes provide distinct advantages of PLD over other vapor deposition methods. Specifically, they enable precise incorporation of the Cs and FA components in the perovskite structure without damage to the organic compounds, while also eliminating the dependency on the volatility of the precursor materials.[39,41] Additionally, the deposition occurs from a plasma plume, which further ensures the controlled delivery of material pulse-by-pulse,[42] homogenous and conformal coverage.[40,43] Previous studies on MHP PLD absorbers have focused on either fully inorganic compositions, such as $CsSnI_3$,[44] $Cs_2AgBiBr_6$,[45] $CsPbBr_3$[46–48] or absorbers containing only organic A-site cations, such as $MAPbI_3$,[42,49] and $MA_xFA_{1-x}PbI_3$, including Cl^- and 2D-passivated $MA_xFA_{1-x}PbI_3$ films.[41,43,50] Here we take a step further to showcase the compositional control of PLD for Cs-FA-based perovskites with in-depth material analysis and the functionality with some proof-of concept solar cells. Furthermore, to reduce substrate-to-substrate variability, to avoid the dependence on substrate properties and formation of photoinactive phases, we employ the approach of template-assisted growth, as introduced in earlier works.[15,16,35]

2. Results and Discussion

The template-assisted growth process using PLD is illustrated in **Figure 1**. In the initial step (a), a lead iodide (PbI_2) film of ≈20 nm is deposited onto a glass/ITO/MeO-2PACz substrate using a stoichiometric PbI_2 target. This seeding layer acts as a template base, reducing substrate-dependent variability during perovskite growth and improving adhesion of organic molecules to the substrate at later stages of growth. In the second step (b), a

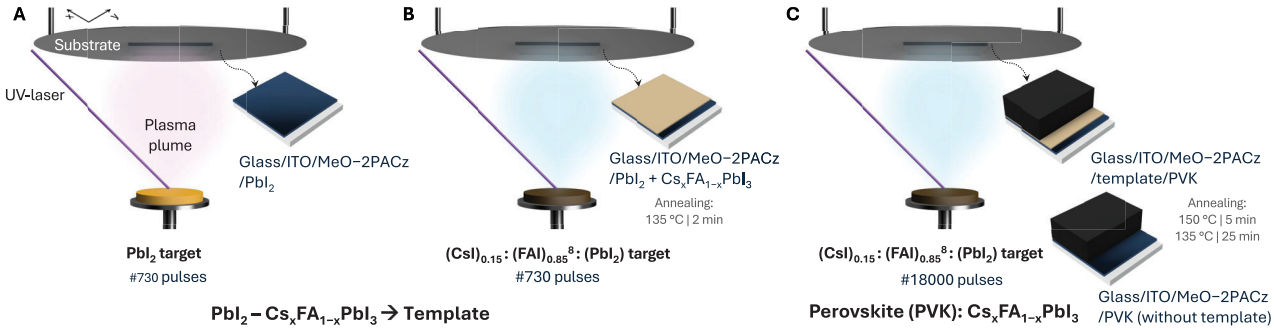

Figure 1. Schematics of the template-assisted growth of $Cs_xFA_{1-x}PbI_3$ by PLD at room temperature. Deposition of A) ≈20 nm of a PbI_2 layer, B) ≈20 nm $Cs_xFA_{1-x}PbI_3$ layer on top of PbI_2 to form the template, and C) ≈650 nm of the complete $Cs_xFA_{1-x}PbI_3$ perovskite (PVK) films, either on the prepared template or directly on the substrate without a template.

≈20 nm cesium formamidinium lead iodide ($Cs_xFA_{1-x}PbI_3$) layer is deposited directly on top of the PbI_2 seeding layer and subsequently annealed at 135 °C for 2 min, forming a crystallization template for the final growth stage. In the final step (c), the bulk $Cs_xFA_{1-x}PbI_3$ perovskite (PVK) layer is deposited either onto the prepared PbI_2 – $Cs_xFA_{1-x}PbI_3$ template, or, for comparison, directly onto the glass/ITO/MeO-2PACz substrate without template. Post-deposition annealing is performed at 150 °C for 5 min, followed by 135 °C for 25 min to finalize crystallization dynamics. Further details of the experimental methodology and growth parameters are provided in the Experimental section.

In the PLD process, achieving the optimal composition and desired phase in the resulting films relies significantly on the quality of the target material.[40] We prepare PLD targets in-house using a mechanochemical approach as reported in our previous studies and described in the experimental section.[41,43,49,50] The precursors, cesium iodide (CsI), formamidinium iodide (FAI) and lead iodide (PbI_2), are mixed in a 0.15 : 0.85 : 1 molar ratio. Following earlier studies, we add an eightfold excess of FAI precursor (relative to PbI_2) to compensate for potential iodide and organic components loss during the PLD process, thus ensuring the desired composition in the final film.[41] **Figure 2A** presents the X-ray diffraction (XRD) pattern of the $Cs_xFA_{1-x}PbI_3$ PLD

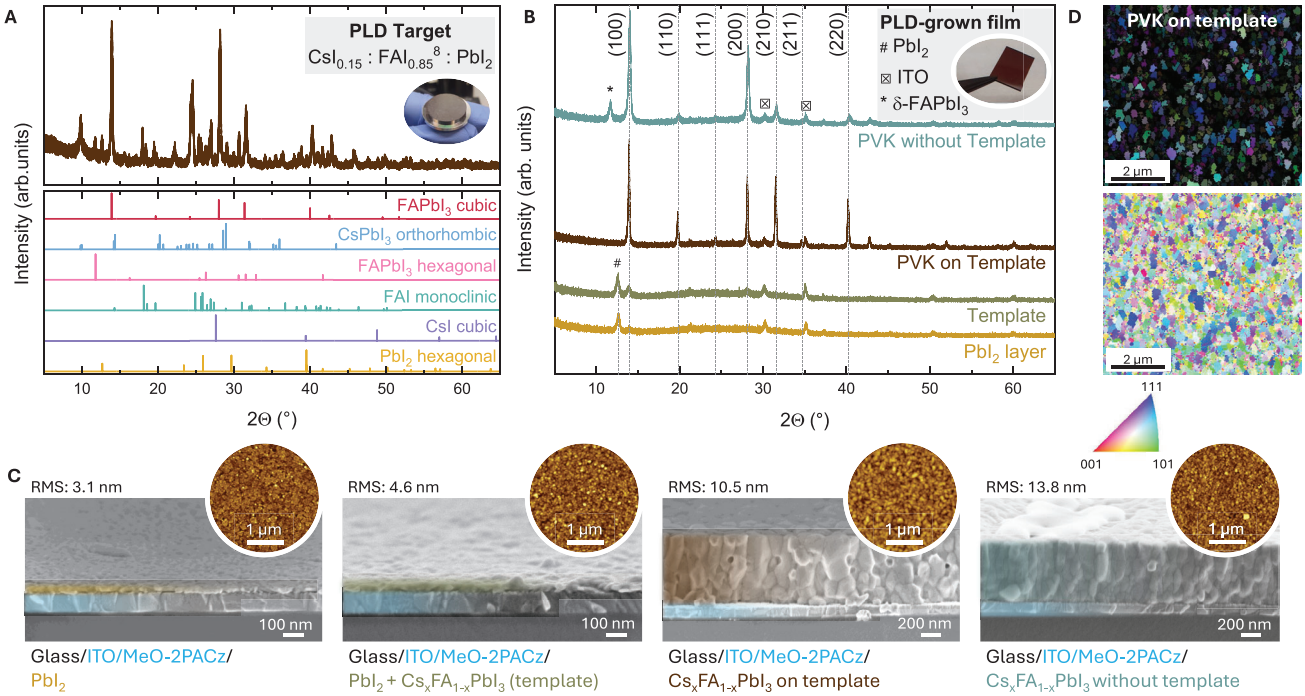

Figure 2. Structural and microstructural properties: A) XRD pattern of a single-source $(CsI)_{0.15} : (FAI)_{0.85}{}^8 : PbI_2$ PLD target, with a photograph of the target shown in the inset; B) XRD patterns of the inorganic PbI_2 layer, PbI_2 – $Cs_xFA_{1-x}PbI_3$ template layer, perovskite layer (PVK) grown on the template and perovskite film without a template (dashed lines indicate peak positions and orientations of the α-$FAPbI_3$ phase); C) Cross-sectional SEM images with false coloring to distinguish distinct layers, and inset AFM topography images for the same samples (scale bars included for reference); D) Inverse pole figure (IPF) with overlaid confidence index (CI) map (top panel) and IPF showing grain orientations of PVK on template films, as indicated by the orientation legend (bottom panel).

target. Unlike previous reports where single-source $Cs_xFA_{1-x}PbI_3$ deposition was achieved using phase-pure powders as a starting material,[23,24] our PLD target consists of a mixture of phases, including unreacted and excess precursors (see Table S2, Supporting Information for reference patterns details). This composition indicates that during mechanosynthesis, a portion of the precursors reacted to form the photoactive cubic (α)-phase, while some converted into the photoinactive hexagonal (δ)-phase, and some of them remained unreacted or in excess. For comparison, the PbI_2 PLD target, prepared directly from PbI_2 precursor, represents a compositionally pure system that exhibits a crystalline structure in the hexagonal phase of PbI_2 (Figure S1, Supporting Information).[51]

The first layer of the template consisting of ≈20 nm of PbI_2 deposited on glass/ITO/MeO-2PACz, also crystalizes in the hexagonal phase (Figure 2B). Upon depositing ≈20 nm of $Cs_xFA_{1-x}PbI_3$ on top of PbI_2 and annealing at 135 °C, a template is formed showing the presence of both PbI_2 and α-$FAPbI_3$ phase (Figure 2B). Finally, a thicker layer of $Cs_xFA_{1-x}PbI_3$ perovskite absorber is deposited on top of the template layer, achieving the desired thickness for device integration (≈650 nm). This film was annealed at 150 °C for 5 min and at 135 °C for 25 min.[16,35] Despite the template layer showing the presence of PbI_2 phase, the resulting perovskite film grown on template shows no trace of excess of PbI_2, indicating a complete reaction between PbI_2 and the rest of the target precursors (Figure 2B). The formation of the cubic α-$FAPbI_3$ phase in the template layer and the subsequent $Cs_xFA_{1-x}PbI_3$ film grown on the template, can be further corroborated with the photoluminescence spectra presenting a primary emission peak at 1.58 eV (Figure S2, Supporting Information). The presence of a single phase for the templated growth suggests that the template provides a foundation that further nucleates the growth of the subsequent perovskite layer, promoting crystallization in the cubic (α)-phase. Conversely, films grown directly on a glass/ITO/MeO-2PACz substrate, without the template layer, resulted in a formation of mixed α- and δ-phases in the $Cs_xFA_{1-x}PbI_3$ films (Figure 2B). This mixed-phase composition indicates that the absence of a templating layer leads to non-uniform crystallization, as the substrate alone does not provide sufficient structural support or nucleation sites to stabilize the photoactive α-phase. Formation of photoinactive δ-phase, likely due to uneven nucleation and growth dynamics that favor phase segregation at the A-site cation level (Cs^+ and FA^+) is primarily attributed to the non-uniform sticking of the organohalide salt during deposition. In contrast, in the case of templated growth, this issue is mitigated, as the template provides a consistent layer that facilitates uniform adhesion and integration of the perovskite components, similar to the sequential processes.[52] Additionally, the absence of the δ-phase in the thinner films and its formation in the thicker films is consistent with recent findings in the literature. DFT calculations by Feeney et al. suggest that the α-phase of $FAPbI_3$ is favored during the early stages of growth, while the δ-phase becomes thermodynamically preferred after reaching a critical thickness.[19] This phenomenon, along with its implications on the interplay of kinetic and thermodynamic stabilization, will be discussed in greater detail later in the manuscript. Although the PLD target contains multiple perovskite phases and precursors, the resulting films, whether templated or not, show only the perovskite phases, confirming that the PLD process facilitates the integration of the perovskite components, as well as the successful reaction at the growth front of the film between the two types of A-site cations (Cs^+ and FA^+) and the PbI_2. Based on the XRD peak position of the perovskite phase at ~14° 2Θ, the expected Cs content in the films is ≈0.2,[11] as it will be confirmed with compositional analysis below.

To evaluate film coverage, quality, and surface morphology, we characterized the samples using scanning electron microscopy (SEM) and atomic force microscopy (AFM) (Figure 2C). Cross-sectional SEM images and AFM topography scans confirm the formation of dense, compact layers for both the PbI_2 seed layer and the $Cs_xFA_{1-x}PbI_3$ template layer. This contrasts with earlier reports, where a thermally evaporated inorganic halide layers of similar thickness exhibited island-like growth for the same substrate configuration.[34] Phase imaging AFM scans in Figure S3 (Supporting Information) further confirm the complete coverage achieved by PLD. In addition to the seed and template layers, the thicker $Cs_xFA_{1-x}PbI_3$ perovskite films grown for device integration exhibit smooth, continuous surfaces without large voids, indicative of high-quality film growth. The root mean square (RMS) roughness of the films increases with layer thickness: 3 nm for the PbI_2 film, 4.6 nm for the $Cs_xFA_{1-x}PbI_3$ template, and 10.5 nm for the final $Cs_xFA_{1-x}PbI_3$ perovskite film grown on template. Notably, the $Cs_xFA_{1-x}PbI_3$ grown without the template shows slightly higher RMS roughness (13.8 nm) compared to the templated-grown film, indicating the template's role in improving surface smoothness and film uniformity. Furthermore, X-ray photoelectron spectroscopy (XPS) survey measurements of all prepared thin-films revealed no signals from the underlying ITO substrate (Figure S4, Supporting Information). This confirms a completely pinhole-free and dense coverage, as any photoelectron pathway from the substrate would result in detectable signals. Electron backscatter diffraction (EBSD) analysis of the PVK films grown on the template revealed the formation of polycrystalline films with no preferential orientation. Notably, EBSD measurements were only successful for the templated films, as the non-templated films did not provide sufficient signal to detect crystalline orientations. The confidence index (CI) mapping (Figure 2D, top panel) indicates that brighter grains correspond to higher-quality EBSD patterns within the dataset. These grains were identified as belonging to the {111} or {101} family of planes, as determined from the inverse pole figure (IPF) and the orientation legend (Figure 2D, bottom panel, Figure S5A, Supporting Information). However, the primary peak orientations acquired from XRD measurements of templated films (Figure 2B) correspond to the {100} family of planes. We hypothesize that this mismatch arises from the instability of {100} grains of Cs-FA based MHPs under the electron beam. By the time the EBSD signal is acquired, the {100} grains may have already degraded (Figure S5, Supporting Information). This instability could also explain why EBSD patterns could not be recorded for non-templated PVK films, which exhibit preferential orientation along the (100) plane. These findings open the door to further investigations to validate this hypothesis and explore its implications.

To assess if the composition is the same for the templated and non-templated growth, we conducted X-ray fluorescence (XRF) measurements on both the PLD targets and the corresponding deposited films. XRF analysis allowed for quantification of the

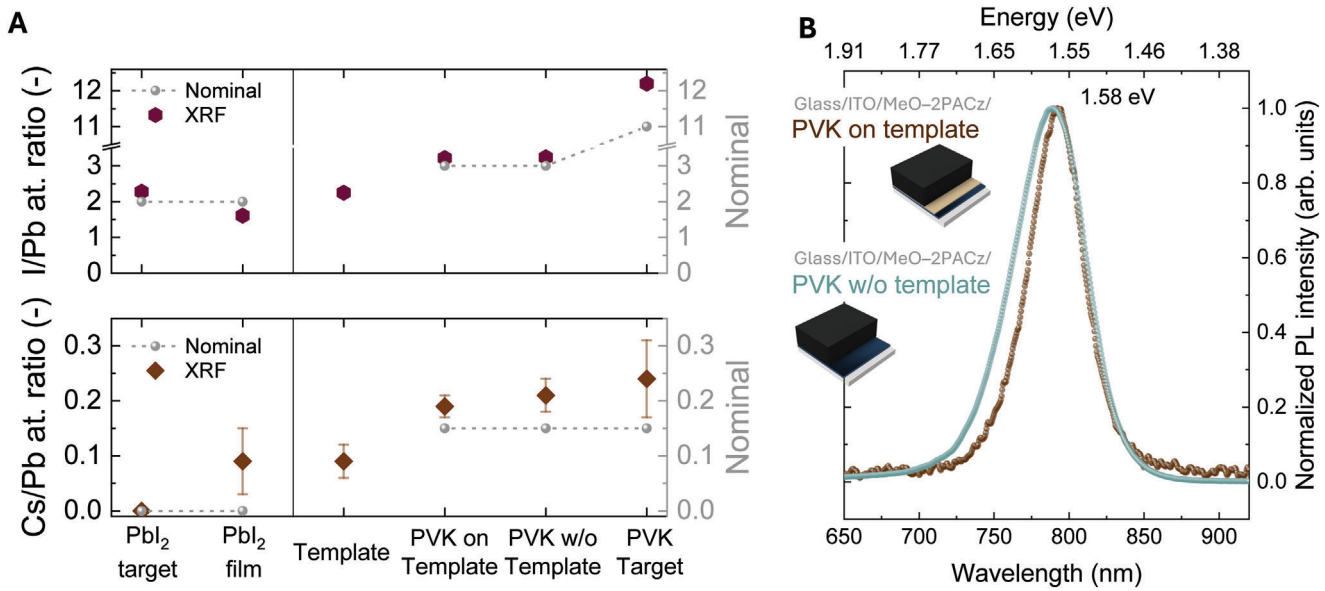

Figure 3. Compositional and optical characterization: A) XRF compositional characterization of PbI_2 and $Cs_xFA_{1-x}PbI_3$ PLD targets and thin-films: top panel represents I/Pb atomic ratio, bottom panel Cs/Pb atomic ratio, points represent average values, while error bars include statistical and systematic error (PVK stands for perovskite); B) Steady-state photoluminescence spectra of $Cs_xFA_{1-x}PbI_3$ PVK films grown with and without template (transmittance, reflectance and absorptance are presented in Figure S8, Supporting Information).

elemental ratios of elements with atomic number, $Z > 11$, enabling direct comparison between the nominal and achieved film compositions.[53,54] Detailed composition values can be found in Table S3 (Supporting Information). and are graphically presented in **Figure 3**A, with I/Pb and Cs/Pb atomic ratio presented in top and bottom panel, respectively. The PbI_2 target, prepared from pure chemical, does not contain cesium, as reflected in the Cs/Pb atomic ratio of 0 in Figure 3A (bottom left panel). Nonetheless, traces of Cs were detected in the PbI_2 seed films, likely arising from the cross-contamination during sample shipping or XRF measurement. The absence of significant Cs incorporation in the PbI_2 seed layer can be further confirmed with the XRD patterns (Figure S1, Supporting Information) and photoluminescence (PL) spectra (Figure S2, Supporting Information), where no Cs-containing phases were observed. The I/Pb atomic ratio for both the PbI_2 target and the PbI_2 films aligns closely with the nominal value of 2, as shown in Figure 3A (top left panel). On the other side, the PVK target, with a nominal composition of $CsI_{0.15}$: $(FAI_{0.85})^8$:(PbI_2) exhibits, as expected, a large excess of iodine, with an I/Pb atomic ratio of ≈12 due to the eightfold excess of FAI used in target preparation. In contrast, both templated and non-templated films, show a reduced I/Pb ratio of ≈3, aligning with the expected nominal stoichiometry of the final perovskite phase (Figure 3A, top right panel). Similarly, the Cs/Pb atomic ratio in the PVK target and deposited films is ≈0.2, closely matching the nominal value of 0.15 within error bars (Figure 3A, bottom right panel). The template layer composition lies between that of the PbI_2 seed layer and the final perovskite films, with an I/Pb ratio of ≈2 and a Cs/Pb ratio of ≈0.1. While no nominal reference value exists for the template, its intermediate composition suggests partial conversion toward the perovskite phase. This observation is supported by PL and XRD measurements, which reveal the presence of a perovskite phase in the template layer (Figure 2B; Figure S2, Supporting Information, respectively).

Notably, both templated and non-templated films display identical I/Pb and Cs/Pb atomic ratios, correlating with a shared bandgap of 1.58 eV, as shown in Figure 3B. This suggests that the template does not significantly influence the overall composition during PLD, as the transfer of elements from the target to the substrate appears stable and consistent across both templated and non-templated films. The results further demonstrate the stoichiometric and controlled transfer of inorganic species from the target to the films during PLD. Notably, the perovskite PLD target remains compositionally unaltered even after multiple deposition cycles, as evidenced in Figure S6 (Supporting Information). This stability highlights a key advantage of the PLD process, where the target composition remains robust over time, ensuring reliable and reproducible film properties and reduced material use. The surface photovoltage (SPV) data presented in Figure S7 (Supporting Information) show an evenly distributed photovoltage across the perovskite film grown on the template, further confirming the high quality and compositional homogeneity of the fabricated templated $Cs_xFA_{1-x}PbI_3$ perovskite film. Consequently, while the template plays a role in crystallization control, it does not impact the elemental composition, underscoring robustness of PLD process in achieving controlled near-stoichiometric transfer of the inorganic species. According to the XRF analysis, the composition of our absorber approximates $Cs_{0.2}FA_{0.8}PbI_3$. As confirmed by XRF, the composition of our perovskite absorber is within FA-rich conditions (Cs content, $x \approx 0.2$), where both α- and δ-phase formation are thermodynamically possible. This explains the difference in crystallization observed for templated and non-templated $Cs_xFA_{1-x}PbI_3$ films.[11] The observed phase behavior in templated versus non-templated $Cs_xFA_{1-x}PbI_3$ films reflects the interplay of kinetic and thermodynamic stabilization

mechanisms in perovskite formation.[55] Therefore, kinetic considerations are equally critical for phase stabilization. Kinetic trapping enables the stabilization of phases that may not be the most thermodynamically favorable but arise due to slower nucleation and growth kinetics.[56] For example, during the deposition of $Cs_xFA_{1-x}PbI_3$ films on non-templated substrates, uneven nucleation dynamics, and slower reaction rates can lead to the formation of mixed phases or even a non-equilibrium δ-phase.[19] In contrast, the use of a template layer facilitates uniform nucleation and accelerates the crystallization process. The crystallization of templated films begins from the inorganic framework, which plays a crucial role in enabling kinetic trapping of the cubic α-phase.[19,26,55] This mechanism ensures optimized film composition and structure, even under deposition conditions that would otherwise favor δ-phase formation. These observations underscore the critical importance of processing strategy in achieving energetically favorable and stable phase conditions.[10,57]

Additionally, we performed X-ray photoelectron spectroscopy (XPS) analysis. However, based on complementary XRF measurements of samples introduced and not introduced to the XPS chamber, a degradation under the required ultra-high vacuum (UHV) conditions was observed. UHV degradation is reported to often occur for organo-halide metal perovskites even without additional heating from the probe beam.[58] As a result, the analysis was restricted to the qualitative discussion of the observed elements presented in Figure S4 (Supporting Information).

As noted earlier, both templated and non-templated films have identical bandgaps of ≈1.58 eV, extracted from steady-state PL spectra in Figure 3B. It is important to highlight that the templated films display a slight redshift in the PL peak compared to the non-templated films. This small redshift may result from potential compositional variations, as indicated by the error bars in the XRF spectra, or from strain effects, which are known to alter the bandgap of perovskite materials.[42,59] Figure S8 (Supporting Information) presents the Urbach energy (E_U) calculation from the PL data.[60] A decrease in E_U from 16.6 to 14.7 meV for non-templated and templated films, respectively, suggests improved material quality, reflecting enhanced structural order and further confirming observed structural differences (Figure 2B). Furthermore, templated PVK films exhibit enhanced optical absorptance compared to the non-templated films, which can be attributed to differences in film thickness (700 nm for PVK on template and 630 nm for PVK w/o template, Figure 2C) and improved structural characteristics induced by the template. For a comprehensive analysis, the transmission, reflectance, and absorptance data are provided in Figure S9 (Supporting Information).

Following a structural, compositional, and optical characterization, we integrated the studied perovskite films into a solar cell architecture consisting of an ITO/MeO-2PACz/PVK/MgF_2/C_{60}/BCP/Ag stack, where PVK designates perovskite film without or with template layer. The photovoltaic parameters are summarized in Figure S10 (Supporting Information). Although the absorbers demonstrated overall good optoelectronic properties, devices fabricated from films without template, were non-functional, likely due to the presence of the δ-phase, which may have contributed to shunting and prevented current extraction.[10,61] Other potential causes include an excess of organics (as suggested by Feeney et al.)[62] but in an amorphous state as they were not detected by XRD (Figure 2B). Thus, we focused on templated films, optimizing devices, and scaling up their active area. **Figure 4** summarizes the performance of templated $Cs_xFA_{1-x}PbI_3$ solar cells fabricated by PLD. A schematic representation of the device architecture, detailing the stack layout and substrate dimensions is presented in Figure 4A. The configuration includes ITO/MeO-2PACz/PVK on template/MgF_2/C_{60}/BCP/Ag for devices with an active area of 0.01 cm^2 on a 2.0 cm × 1.5 cm substrate, and ITO/MeO-2PACz/PVK on template/C_{60}/ALD-SnO_x/Ag for 0.1 cm^2 devices on a 2.5 cm × 2.5 cm substrate. The distribution of photovoltaic (PV) parameters, including short-circuit current density (J_{sc}), open-circuit voltage (V_{oc}), fill factor (*FF*), and power conversion efficiency (*PCE*), is shown in panel Figure 4B. As expected, increasing the device size led to a decrease in fill factor, likely due to increased series resistance and current collection challenges over larger areas. However, by replacing the thermally evaporated MgF_2/C_{60}/BCP/Ag (used for 0.01 cm^2) with C_{60}/ALD-SnO_x/Ag for the 0.1 cm^2 device, the average V_{oc} improved by > 50 mV. This improvement can be attributed to better energy band alignment in the C_{60}/ALD-SnO_x/Ag top-electrode stack. Representative current density-voltage (*J-V*) curves of the champion devices are shown in Figure 4C. The best-performing device with an active area of 0.01 cm^2 achieved a PCE of 14.06%, while the champion 0.1 cm^2 device demonstrated a comparable performance of 12.91%. The PV parameters of the fabricated devices summarized in Table S4 (Supporting Information), and the representative external quantum efficiency (*EQE*) spectra presented in Figure S11 (Supporting Information), confirm that the short-circuit current density values are consistent with those obtained from the *J–V* measurements. Additionally, the shelf-life stability of the templated solar cells was monitored over time, as shown in Figure S12 (Supporting Information). Notably, the PCE remained stable for over 3000 h after fabrication, with the devices stored under an N_2 atmosphere and measured in air under ambient conditions. This demonstrates the excellent long-term stability of the templated $Cs_xFA_{1-x}PbI_3$ films under controlled environment. Despite the overall good absorber properties and low Urbach energy, the device performance remains moderate compared to the state-of-the-art vapor deposited MHPs with similar composition (as shown in Table S1, Supporting Information). As noted in previous studies, low-E_U materials may still contain energetically deep states due to localized defects at interfaces and grain boundaries, which can lead to nonradiative recombination and limit device performance.[60,63] To explore whether these factors were limiting our devices, we performed light intensity-dependent V_{oc} measurements and light-soaking test (Figure S13, Supporting Information). Analysis of the light intensity – V_{oc} data, both before and after light soaking, revealed an ideality factor of ≈2, suggesting that recombination is dominated by trap-assisted mechanisms within the bulk material or at interfaces.[64] Such recombination is indicative of a significant density of defect states, a characteristic often seen in vapor-deposited perovskites.[14,65] Based on these findings, we attribute the moderate device performance primarily to defect states within the absorber and at the interfaces. In addition, short-term maximum power point (MPP) tracking (Figure S14, Supporting Information) demonstrated that unencapsulated cells remained operational but exhibited a gradual performance decline over time. However, following prolonged light exposure

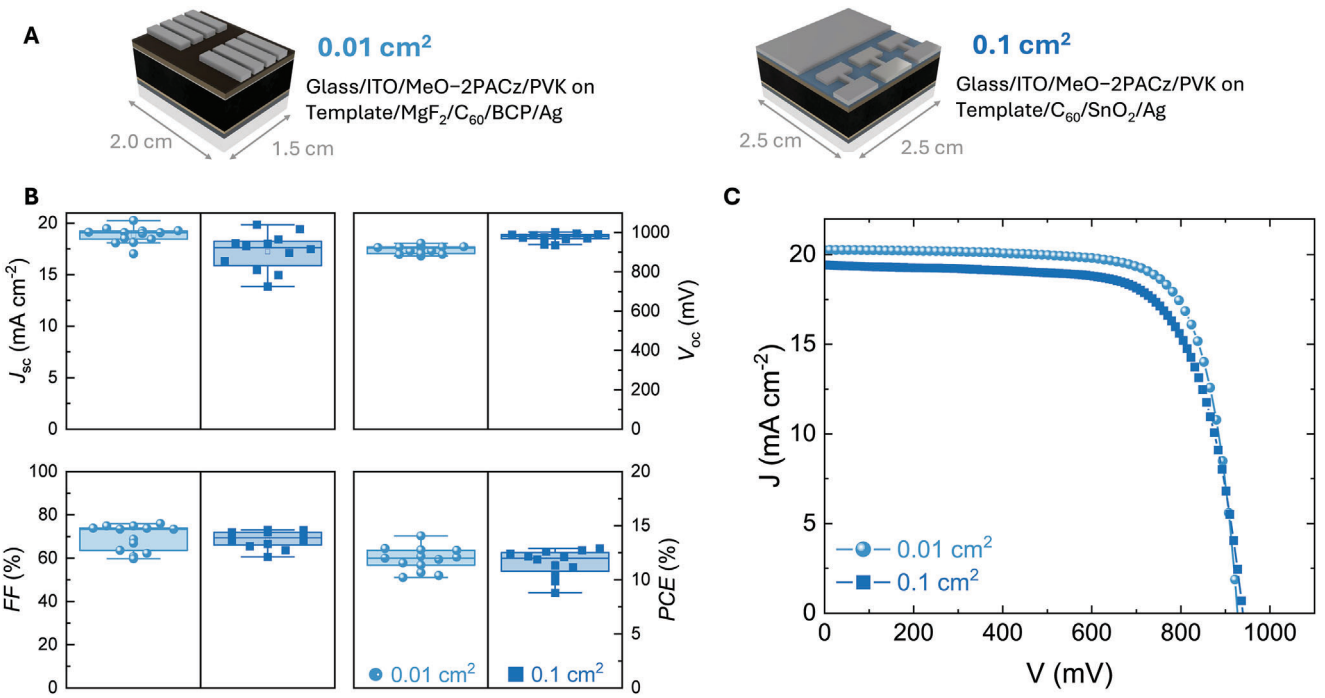

Figure 4. Templated $Cs_xFA_{1-x}PbI_3$ PLD solar cells for A) Schematic representation and stack layout of devices with 0.01 and 0.1 cm^2 active area, B) Distribution of photovoltaic parameters, and C) Current density-voltage (*J–V*) curves of champion devices.

and subsequent dark recovery, *J–V*, XRD, and PL measurements indicate a recovery of PV performance to levels comparable to pre-stress conditions (Figure S15A, Supporting Information). The main loss in performance arises from the *FF*, indicating the presence of increased non-ideal charge transport or recombination at interfaces under prolonged illumination. In contrast, V_{oc} remains rather constant, indicating that the bulk properties of the material and the overall band alignment are not significantly affected by light stress. This was further corroborated by the stability of the PL peak position throughout the light-soaking test which indicated that the bandgap and emission characteristics of the solar cells remained unaffected. Additionally, no evidence of degradation-related secondary phases, such as δ-phase $Cs_xFA_{1-x}PbI_3$, orthorhombic phase transitions, or increased PbI_2 peaks, was observed. These findings confirm the compositional homogeneity and robust stability of the templated $Cs_xFA_{1-x}PbI_3$ films under extended light exposure (Figure S15B, Supporting Information). While our templated approach preserves the material's integrity, bulk, and interface improvements are necessary to minimize defect density and enhance performance relative to the detailed balance limit of an absorber with the same bandgap (Figure S16, Supporting Information).[66,67] Strategies to mitigate such defects in vapor-processed MHPs are the use of chlorine-based compounds as crystallization agents or bulk and surface passivation strategies.[22,34,50,65,68,69] However, this is yet to be explored for templated PLD absorbers.

As the next step and to confirm the conformality of PLD, we deposited $Cs_xFA_{1-x}PbI_3$ on textured silicon wafers coated with ITO (Si-wafer) (**Figure 5**). The XRD patterns highlight the differences between templated and non-templated films, which are even more pronounced compared to planar substrates (Figure 5A). Films deposited without a template exhibit a prominent peak at 11.7° 2Θ, corresponding to the δ-phase and peaks between 24° and 28° 2Θ, which correspond to kinematically forbidden reflections of the cubic phase.[61,70] In contrast, the templating approach results in an α-phase $Cs_xFA_{1-x}PbI_3$ with minor presence of unreacted PbI_2 (peak at 12.6° 2Θ). The PL spectra (Figure 5B) follow the trend and conclusions made for planar substrates, with films exhibiting the same bandgap (1.58 eV). Furthermore, a conformal coverage of the highly textured Si-wafer substrate was evidenced for both templated and non-templated films (Figure 5C).

For MHPs to reach practical application potential, achieving high deposition rates, while maintaining the absorber quality are essential steps for scaling up the process and increasing throughput.[14,22,71,72] In PLD, the deposition rate can be easily tuned by increasing the laser pulse repetition rate (i.e., frequency).[39,40,73] Here, we varied the laser frequency from 4 Hz – 8 Hz – 16 Hz. The respective deposition rates achieved were 4, 9, and 18 nm min^{-1} according to the cross-sectional SEM images of templated films grown with different frequencies on the textured Si-wafers (Figure 5D). Thicknesses and deposition time are summarized in Table S5 (Supporting Information). Notably, increasing the deposition rates did not affect the morphology, coverage, or overall quality of perovskite absorbers. Structural (Figure 5E) and optical (Figure 5F) analyses further confirmed these findings, with the XRD pattern indicating consistent absorber quality and orientation across all tested deposition rates, with only a minor presence of PbI_2 at the highest deposition rate (18 nm min^{-1}) which could be beneficial for actual device configuration.[70] These results highlight the efficacy of templated approach in achieving phase-pure, well-oriented films, even on textured surfaces at high deposition rates.

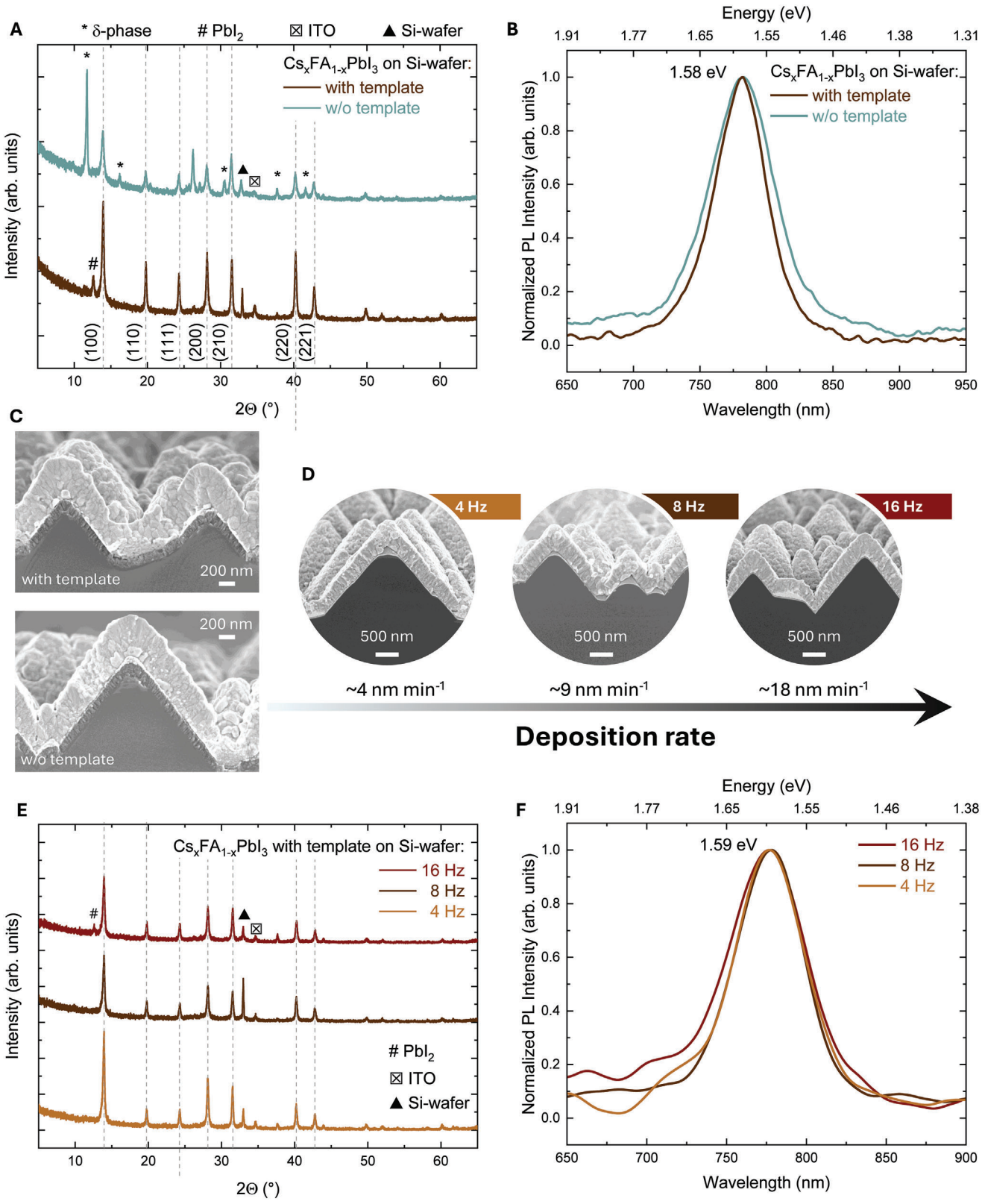

Figure 5. Structural, morphological, and optical characteristics of $Cs_xFA_{1-x}PbI_3$ films grown on textured silicon wafers (Si-wafer): A) XRD patterns, B) PL spectra, and C) cross-sectional SEM images of perovskite films with and without template; D) cross-sectional SEM images, E) XRD pattern, and F) PL spectra of templated perovskite grown at different laser frequencies, i.e. deposition rates.

Additionally, bandgap values remain stable across rates, underscoring the repeatability of this method. The insights gained from PLD, particularly regarding stoichiometric transfer, template-assisted growth, and controlled crystallization, can be directly translated to other scalable vapor deposition techniques. With this, we believe that PLD serves as a valuable platform for advancing vapor deposition techniques of mixed cation MHPs.

3. Conclusion

In conclusion, our study demonstrates that template-assisted PLD enables the controlled growth of high-quality $Cs_{0.2}FA_{0.8}PbI_3$ perovskite films with uniform, dense coverage on both planar and textured substrates. Compositional analysis confirms near-stoichiometric transfer and stable Cs and FA ratios, with templated growth proving critical to obtaining phase-pure, photoactive films. The template layer not only supports improved crystallization but also enables preserving the high-quality film properties even at increased deposition rates. A proof-of-concept solar cell achieved an efficiency above 14%, highlighting the effectiveness of this approach in enhancing perovskite device performance. With this method, we aim to contribute to ongoing efforts to refine and optimize physical vapor deposition techniques.

4. Experimental Section

Target Preparation Process: CsI (99.999%, *abcr*), FAI (>99.99%, *Greatcell Solar*), and PbI_2 (99.999%, *Sigma–Aldrich*) powders were weighed in a nitrogen-filled glovebox and loaded into zirconia-coated vials (*Retsch GmbH*) with zirconia beads. The precursor ratio for CsI : FAI : PbI_2 was set at 0.15 : 0.85 : 1, with FAI added in 8 times excess to account for its volatility during the PLD process. The vials were sealed and mixed overnight using an *in-house* built rotary ball miller. The powders were separated from the beads and loaded into a 1-inch die for pressing. Pressing was conducted in an *Atlas Automatic Lab Press* under applied pressure of 195 MPa for 30 min. A stoichiometric PbI_2 target was prepared from high-purity PbI_2 powder, processed in a similar manner. The targets were then mounted on a holder for the PLD chamber and used for multiple depositions.

Perovskite Film Growth with Pulsed Laser Deposition (PLD): PLD of halide perovskites was films was carried out using a custom-made PLD setup, developed by *DEMCON Twente Solid State Technology*. All depositions were performed at room temperature within a controlled, low-pressure environment, with baseline pressures maintained in the 10^{-7} mbar range. A 248 nm KrF excimer laser (*Coherent COMPex*) served as the ablation source, with an output energy of 7.8 mJ per pulse focused onto a 2.41 mm^2 spot. To ensure uniform film coverage across the substrate, the PLD setup employed a heater scanning option, enabling even deposition over an area of 36 mm × 36 mm. The scanning was conducted at a step size of 2 mm and a speed of 2 mm s^{-1}. The deposition pressure was set to $2 \cdot 10^{-2}$ mbar (argon atmosphere), and film thickness was controlled by adjusting the laser pulse frequency and the total number of pulses. For the template layers, a ≈20 nm PbI_2 and a ≈20 nm $Cs_xFA_{1-x}PbI_3$ layer were each deposited with a pulse count of 730 and a frequency of 2 Hz. Post-deposition, the films were transferred from the deposition chamber to a glovebox and annealed at 135 °C for 2 min. Subsequently, the samples were reintroduced to the PLD chamber for the deposition of a thicker $Cs_xFA_{1-x}PbI_3$ layer. This layer was deposited with 18 000 pulses at a frequency of 8 Hz, resulting in a deposition time of 37.5 min for a film thickness of ≈650 nm (all thicknesses determined from cross-sectional SEM images). The film was then annealed at 150 °C for 5 min, followed by 25 min at 135 °C.[16,29,35] For depositions on textured silicon heterojunction cells, to account for geometrical differences, the pulse count was increased to 1460 for the template layers and to 22 000 for the thick $Cs_xFA_{1-x}PbI_3$ layer. To achieve different deposition rates, the frequency was varied from 4, 8 to 16 Hz, while the rest of process parameters remained the same.

Supporting Information

Supporting Information is available from the Wiley Online Library or from the author.

Acknowledgements

This project was funded by the European Research Council (ERC) under the European Union's Horizon 2020 Research and Innovation Program (CREATE, Grant Agreement No.852722). S.K., M.M.M., K.A., and C.M.W. acknowledge additional funding from the European Union's Horizon 2020 Research and Innovation Program (VIPERLAB, Grant No. 101006715, VLAB-234-00137). K.A. and C.M.W. further acknowledge support from the Horizon 2020 Research and Innovation Program (TRIUMPH, Grant No. 101075725), the Swiss National Science Foundation (A3P, 40B2-0_1203626), the Swiss Federal Office of Energy (PERSISTARS), the Services Industriels de Genève (SIG) and the ETH Domain through an AM grant (AMYS). The authors would like to acknowledge M. Smithers for SEM imaging, D. Post, J. Valkenhoef, and D. Monteiro Cunha for technical support.

Conflict of Interest

The authors declare no conflict of interest.

Data Availability Statement

The data that support the findings of this study are available from the corresponding author upon reasonable request.

Keywords

$Cs_xFA_{1-x}PbI_3$, pulsed laser deposition (PLD), templated growth

Received: December 21, 2024
Revised: February 16, 2025
Published online:

[1] A. Kojima, K. Teshima, Y. Shirai, T. Miyasaka, *J. Am. Chem. Soc.* **2009**, *131*, 6050.
[2] C. C. Stoumpos, C. D. Malliakas, M. G. Kanatzidis, *Inorg. Chem.* **2013**, *52*, 9019.
[3] G. E. Eperon, S. D. Stranks, C. Menelaou, M. B. Johnston, L. M. Herz, H. J. Snaith, *Energy Environ. Sci.* **2014**, *7*, 982.
[4] Y. Deng, S. Xu, S. Chen, X. Xiao, J. Zhao, J. Huang, *Nat. Energy.* **2021**, *6*, 633.
[5] *LMPV, A. M. O. L. F., Detailed Balance (DB) Charts*, **2024**, https://amolf.nl/research/sustainable-energy-materials/detailed-balance-charts.
[6] A. Polman, M. Knight, E. C. Garnett, B. Ehrler, W. C. Sinke, *Science.* **2016**, *352*, aad4424.
[7] J. A. Vigil, A. Hazarika, J. M. Luther, M. F. Toney, *ACS Energy Lett.* **2020**, *5*, 2475.

[8] M. M. Byranvand, C. Otero-Martínez, J. Ye, W. Zuo, L. Manna, M. Saliba, R. L. Z. Hoye, L. Polavarapu, *Adv. Opt. Mater.* **2022**, *10*, 2200423.
[9] Z. Li, M. Yang, J.-S. Park, S.-H. Wei, J. J. Berry, K. Zhu, *Chem. Mater.* **2015**, *28*, 284.
[10] L. T. Schelhas, Z. Li, J. A. Christians, A. Goyal, P. Kairys, S. P. Harvey, D. H. Kim, K. H. Stone, J. M. Luther, K. Zhu, V. Stevanovic, J. J. Berry, *Energy Environ. Sci.* **2019**, *12*, 1341.
[11] S. Li, Y. Jiang, J. Xu, D. Wang, Z. Ding, T. Zhu, B. Chen, Y. Yang, M. Wei, R. Guo, Y. Hou, Y. Chen, C. Sun, K. Wei, S. M. H. Qaid, H. Lu, H. Tan, D. Di, J. Chen, M. Gratzel, E. H. Sargent, M. Yuan, *Nature.* **2024**, *635*, 82.
[12] M. A. Green, E. D. Dunlop, M. Yoshita, N. Kopidakis, K. Bothe, G. Siefer, D. Hinken, M. Rauer, J. Hohl-Ebinger, X. Hao, *Prog. Photovoltaics.* **2024**, *32*, 425.
[13] P. Du, L. Wang, J. Li, J. Luo, Y. Ma, J. Tang, T. Zhai, *Adv. Opt. Mater.* **2021**, *10*, 2101770..
[14] T. Abzieher, D. T. Moore, M. Roß, S. Albrecht, J. Silvia, H. Tan, Q. Jeangros, C. Ballif, M. T. Hoerantner, B.-S. Kim, H. J. Bolink, P. Pistor, J. C. Goldschmidt, Y.-H. Chiang, S. D. Stranks, J. Borchert, M. D. McGehee, M. Morales-Masis, J. B. Patel, A. Bruno, U. W. Paetzold, *Energy Environ. Sci.* **2024**, *17*, 1645.
[15] K. L. Heinze, P. Wessel, M. Mauer, R. Scheer, P. Pistor, *Mater. Adv.* **2022**, *3*, 8695.
[16] S. Yan, J. B. Patel, J. E. Lee, K. A. Elmestekawy, S. R. Ratnasingham, Q. Yuan, L. M. Herz, N. K. Noel, M. B. Johnston, *ACS Energy Lett.* **2023**, *8*, 4008.
[17] Q. Yuan, K. B. Lohmann, R. D. J. Oliver, A. J. Ramadan, S. Yan, J. M. Ball, M. G. Christoforo, N. K. Noel, H. J. Snaith, L. M. Herz, M. B. Johnston, *ACS Appl. Mater. Interfaces.* **2023**, *15*, 772.
[18] K. L. Heinze, T. Schulz, R. Scheer, P. Pistor, *physica status solidi.* **2024**, *221*, 2300690.
[19] T. Feeney, J. Petry, A. Torche, D. Hauschild, B. Hacene, C. Wansorra, A. Diercks, M. Ernst, L. Weinhardt, C. Heske, G. Gryn'ova, U. W. Paetzold, P. Fassl, *Matter.* **2024**, *7*, 2066.
[20] J. Feng, Y. Jiao, H. Wang, X. Zhu, Y. Sun, M. Du, Y. Cao, D. Yang, S. Liu, *Energy Environ. Sci.* **2021**, *14*, 3035.
[21] H. Li, J. Zhou, L. Tan, M. Li, C. Jiang, S. Wang, X. Zhao, Y. Liu, Y. Zhang, Y. Ye, W. Tress, C. Yi, *Sci. Adv.* **2022**, *8*, eabo7422.
[22] N. Rodkey, I. Gomar-Fernandez, F. Ventosinos, C. Roldan-Carmona, L. J. A. Koster, H. J. Bolink, *ACS Energy Lett.* **2024**, *9*, 927.
[23] N. Klipfel, M. P. U. Haris, S. Kazim, A. A. Sutanto, N. Shibayama, H. Kanda, A. M. Asiri, C. Momblona, S. Ahmad, M. K. Nazeeruddin, *J. Mater. Chem. C.* **2022**, *10*, 10075.
[24] M. Hernández, M. Pacio, H. Juárez, L. E. Serrano, A. Pacio, *J. Phys.: Conf. Ser.* **2024**, *2699*, 012019.
[25] A. F. Castro-Mendez, F. Jahanbakhshi, D. K. LaFollette, B. J. Lawrie, R. Li, C. A. R. Perini, A. M. Rappe, J. P. Correa-Baena, *J. Am. Chem. Soc.* **2024**, *146*, 18459.
[26] S. Kralj, M. Morales-Masis, *Matter.* **2024**, *7*, 3238.
[27] Z. Li, M. Wu, L. Yang, K. Guo, Y. Duan, Y. Li, K. He, Y. Xing, Z. Zhang, H. Zhou, D. Xu, J. Wang, H. Zou, D. Li, Z. Liu, *Adv. Funct. Mater.* **2023**, *33*, 202212606.
[28] M. Roß, S. Severin, M. B. Stutz, P. Wagner, H. Köbler, M. Favin-Lévêque, A. Al-Ashouri, P. Korb, P. Tockhorn, A. Abate, B. Stannowski, B. Rech, S. Albrecht, *Adv. Energy Mater.* **2021**, *11*, 2101460.
[29] Y. H. Chiang, M. Anaya, S. D. Stranks, *ACS Energy Lett.* **2020**, *5*, 2498.
[30] Y. H. Jia, S. Neutzner, Y. Zhou, M. Yang, J. M. F. Tapia, N. Li, H. Yu, J. Cao, J. P. Wang, A. Petrozza, C. P. Wong, N. Zhao, *Adv. Funct. Mater.* **2019**, *30*, 1906875.
[31] M. Ross, L. Gil-Escrig, A. Al-Ashouri, P. Tockhorn, M. Jost, B. Rech, S. Albrecht, *ACS Appl. Mater. Interfaces.* **2020**, *12*, 39261
[32] S. Olthof, K. Meerholz, *Sci. Rep.* **2017**, *7*, 40267.
[33] T. Abzieher, T. Feeney, F. Schackmar, Y. J. Donie, I. M. Hossain, J. A. Schwenzer, T. Hellmann, T. Mayer, M. Powalla, U. W. Paetzold, *Adv. Funct. Mater.* **2021**, *31*, 2104482.
[34] V. Škorjanc, A. Miaskiewicz, M. Roß, S. Maniyarasu, S. Severin, M. R. Leyden, P. Holzhey, F. Ruske, L. Korte, S. Albrecht, *ACS Energy Lett.* **2024**, *9*, 5639.
[35] J. Yan, L. S. Stickel, L. van den Hengel, H. Wang, P. R. Anusuyadevi, A. Kooijman, X. Liu, B. Ibrahim, A. Mol, P. Taheri, L. Mazzarella, O. Isabella, T. J. Savenije, *J. Phys. Chem. Lett.* **2023**, *14*, 8787.
[36] D. Prochowicz, M. Saski, P. Yadav, M. Gratzel, J. Lewinski, *Acc. Chem. Res.* **2019**, *52*, 3233.
[37] F. Palazon, Y. El Ajjouri, H. J. Bolink, *Adv. Energy Mater.* **2019**, *10*, 201902499.
[38] Y. Zhang, Y. Wang, X. Yang, L. Zhao, R. Su, J. Wu, D. Luo, S. Li, P. Chen, M. Yu, Q. Gong, R. Zhu, *Adv. Mater.* **2022**, *34*, 2107420.
[39] T. Soto-Montero, M. Morales-Masis, *ACS Energy Lett.* **2024**, *9*, 4199.
[40] R. Eason, *Pulsed Laser Deposition of Thin Films*, John Wiley & Sons, Inc., Hoboken, New Jersey, **2006**.
[41] T. Soto-Montero, S. Kralj, J. S. Gomez, J. W. Wolffs, N. Rodkey, A. P. M. Kentgens, M. Morales-Masis, *Chem. Mater.* **2024**, *36*, 6912.
[42] J. S. Solomon, T. Soto-Montero, Y. A. Birkhölzer, D. M. Cunha, W. Soltanpoor, M. Ledinský, N. Orlov, E. C. Garnett, N. Forero-Correa, S. E. Reyes-Lillo, T. B. Haward, J. R. S. Lilly, L. M. Herz, G. Koster, G. Rijnders, L. Leppert, M. Morales-Masis, *Nat. Synthes.* **2025**, https://doi.org/10.1038/s44160-024-00717-z.
[43] T. Soto-Montero, S. Kralj, W. Soltanpoor, J. S. Solomon, J. S. Gómez, K. P. S. Zanoni, A. Paliwal, H. J. Bolink, C. Baeumer, A. P. M. Kentgens, M. Morales-Masis, *Adv. Funct. Mater.* **2023**, *34*, 2300588.
[44] V. M. Kiyek, Y. A. Birkhölzer, Y. Smirnov, M. Ledinsky, Z. Remes, J. Momand, B. J. Kooi, G. Koster, G. Rijnders, M. Morales-Masis, *Adv. Mater. Interfaces.* **2020**, *7*, 2000162.
[45] N. Rodkey, S. Kaal, P. Sebastia-Luna, Y. A. Birkholzer, M. Ledinsky, F. Palazon, H. J. Bolink, M. Morales-Masis, *Chem. Mater.* **2021**, *33*, 7417.
[46] M. Cesaria, M. Mazzeo, G. Quarta, M. R. Aziz, C. Nobile, S. Carallo, M. Martino, L. Calcagnile, A. P. Caricato, *Nanomaterials.* **2021**, *11*, 3210.
[47] E. Parrat, F. Dupont, F. Templier, *SID Symp. Digest Techn. Papers.* **2024**, *55*, 132.
[48] H. Wang, Y. Wu, M. Ma, S. Dong, Q. Li, J. Du, H. Zhang, Q. Xu, *ACS Appl. Energy Mater.* **2019**, *2*, 2305.
[49] T. Soto-Montero, W. Soltanpoor, S. Kralj, Y. A. Birkholzer, Z. Remes, M. Ledinsky, G. Rijnders, M. Morales-Masis, in *2021 IEEE 48th Photovoltaic Specialists Conf. (PVSC)*, IEEE, Piscataway, NJ **2021**, pp. 1318–1323.
[50] T. Soto-Montero, S. Kralj, R. Azmi, M. A. Reus, J. S. Solomon, D. M. Cunha, W. Soltanpoor, D. S. Utomo, E. Ugur, B. Vishal, M. Ledinsky, P. Müller-Buschbaum, F. Babbe, D. K. Lee, C. M. Sutter-Fella, E. Aydin, S. De Wolf, M. Morales-Masis, *Joule.* **2024**, *8*, 3412.
[51] Q. Zou, G. Zheng, D. Yao, J. Wang, N. Tian, S. Mo, F. Long, *ACS Omega.* **2023**, *8*, 12430.
[52] Q. Guesnay, F. Sahli, C. Ballif, Q. Jeangros, *APL Mater.* **2021**, *9*, 100703.
[53] B. Beckhoff, h. B. Kanngießer, N. Langhoff, R. Wedell, H. Wolff, *Handbook of Practical X-Ray Fluorescence Analysis*, Springer Science & Business Media, Heidelberg, Germany **2006**.
[54] M. Kodur, R. E. Kumar, Y. Luo, D. N. Cakan, X. Li, M. Stuckelberger, D. P. Fenning, *Adv. Energy Mater.* **2020**, *10*, 1903170.
[55] N. Arora, A. Greco, S. Meloni, A. Hinderhofer, A. Mattoni, U. Rothlisberger, J. Hagenlocher, C. Caddeo, S. M. Zakeeruddin, F. Schreiber, M. Graetzel, R. H. Friend, M. I. Dar, *Commun. Mater.* **2022**, *3*, 22.
[56] T. Chen, B. J. Foley, C. Park, C. M. Brown, L. W. Harriger, J. Lee, J. Ruff, M. Yoon, J. J. Choi, S. H. Lee, *Sci. Adv.* **2016**, *2*, 1601650.

[57] L. E. Mundt, F. Zhang, A. F. Palmstrom, J. Xu, R. Tirawat, L. L. Kelly, K. H. Stone, K. Zhu, J. J. Berry, M. F. Toney, L. T. Schelhas, *ACS Energy Lett.* **2021**, *7*, 471.
[58] R. L. Z. Hoye, P. Schulz, L. T. Schelhas, A. M. Holder, K. H. Stone, J. D. Perkins, D. Vigil-Fowler, S. Siol, D. O. Scanlon, A. Zakutayev, A. Walsh, I. C. Smith, B. C. Melot, R. C. Kurchin, Y. Wang, J. Shi, F. C. Marques, J. J. Berry, W. Tumas, S. Lany, V. Stevanović, M. F. Toney, T. Buonassisi, *Chem. Mater.* **2017**, *29*, 1964.
[59] W. Meng, K. Zhang, A. Osvet, J. Zhang, W. Gruber, K. Forberich, B. Meyer, W. Heiss, T. Unruh, N. Li, C. J. Brabec, *Joule.* **2022**, *6*, 458.
[60] E. Ugur, M. Ledinsky, T. G. Allen, J. Holovsky, A. Vlk, S. De Wolf, *J. Phys. Chem. Lett.* **2022**, *13*, 7702.
[61] T. A. S. Doherty, S. Nagane, D. J. Kubicki, Y. K. Jung, D. N. Johnstone, A. N. Iqbal, D. Guo, K. Frohna, M. Danaie, E. M. Tennyson, S. Macpherson, A. Abfalterer, M. Anaya, Y. H. Chiang, P. Crout, F. S. Ruggeri, S. Collins, C. P. Grey, A. Walsh, P. A. Midgley, S. D. Stranks, *Science.* **2021**, *374*, 1598.
[62] A. Farag, T. Feeney, I. M. Hossain, F. Schackmar, P. Fassl, K. Kuster, R. Bauerle, M. A. Ruiz-Preciado, M. Hentschel, D. B. Ritzer, A. Diercks, Y. Li, B. A. Nejand, F. Laufer, R. Singh, U. Starke, U. W. Paetzold, *Adv. Energy Mater.* **2023**, *13*, 2203982.
[63] B. Subedi, C. Li, C. Chen, D. Liu, M. M. Junda, Z. Song, Y. Yan, N. J. Podraza, *ACS Appl. Mater. Interfaces.* **2022**, *14*, 7796.
[64] D. Luo, R. Su, W. Zhang, Q. Gong, R. Zhu, *Nat. Rev. Mater.* **2019**, *5*, 44.
[65] K. B. Lohmann, S. G. Motti, R. D. J. Oliver, A. J. Ramadan, H. C. Sansom, Q. Yuan, K. A. Elmestekawy, J. B. Patel, J. M. Ball, L. M. Herz, H. J. Snaith, M. B. Johnston, *ACS Energy Lett.* **2022**, *7*, 1903.
[66] I. Susic, L. Gil-Escrig, K. P. S. Zanoni, C. Roldan-Carmona, M. Sessolo, H. J. Bolink, *ACS Mater. Lett.* **2023**, *5*, 3299.
[67] Y. H. Chiang, K. Frohna, H. Salway, A. Abfalterer, L. Pan, B. Roose, M. Anaya, S. D. Stranks, *ACS Energy Lett.* **2023**, *8*, 2728.
[68] R. Azmi, E. Ugur, A. Seitkhan, F. Aljamaan, A. S. Subbiah, J. Liu, G. T. Harrison, M. I. Nugraha, M. K. Eswaran, M. Babics, Y. Chen, F. Xu, T. G. Allen, A. U. Rehman, C. L. Wang, T. D. Anthopoulos, U. Schwingenschlogl, M. De Bastiani, E. Aydin, S. De Wolf, *Science.* **2022**, *376*, 73.
[69] Y. Yang, H. Chen, C. Liu, J. Xu, C. Huang, C. D. Malliakas, H. Wan, A. S. R. Bati, Z. Wang, R. P. Reynolds, I. W. Gilley, S. Kitade, T. E. Wiggins, S. Zeiske, S. Suragtkhuu, M. Batmunkh, L. X. Chen, B. Chen, M. G. Kanatzidis, E. H. Sargent, *Science.* **2024**, *386*, 898.
[70] M. Othman, Q. Jeangros, D. A. Jacobs, M. H. Futscher, S. Zeiske, A. Armin, A. Jaffres, A. G. Kuba, D. Chernyshov, S. Jenatsch, S. Zufle, B. Ruhstaller, S. Tabean, T. Wirtz, S. Eswara, J. Zhao, T. J. Savenije, C. Ballif, C. M. Wolff, A. Hessler-Wyser, *Energy Environ. Sci.* **2024**, *17*, 3832.
[71] H. A. Dewi, E. Erdenebileg, D. De Luca, S. G. Mhaisalkar, A. Bruno, *ACS Energy Lett.* **2024**, *9*, 4319.
[72] T. Abzieher, C. P. Muzzillo, M. Mirzokarimov, G. Lahti, W. F. Kau, D. M. Kroupa, S. G. Cira, H. W. Hillhouse, A. R. Kirmani, J. Schall, D. Kern, J. M. Luther, D. T. Moore, *J. Mater. Chem. A.* **2024**, *12*, 8405.
[73] N. A. Shepelin, Z. P. Tehrani, N. Ohannessian, C. W. Schneider, D. Pergolesi, T. Lippert, *Chem. Soc. Rev.* **2023**, *52*, 2294.